



Microstructure Evolution in Additively Manufactured Steel Molds: A Review

Wee King Law, Kok-Cheong Wong, Haoliang Wang, Zhenzhong Sun, and Chin Seong Lim

Submitted: 30 December 2020 / Revised: 9 May 2021 / Accepted: 22 May 2021 / Published online: 18 June 2021

Over the last decade, developments in metal additive manufacturing (AM) have opened up new possibilities in various industries. Current metal AM technologies are now capable of processing a larger selection of metals, including steel mold materials such as H13 and P20. In the injection molding industry, mold makers have implemented metal AM technologies to 3D print steel molds. The main challenge currently faced by mold makers is to 3D print steel molds with mechanical properties that are comparable with conventionally made ones. Research on the microstructure evolution in 3D printed steel molds provide the necessary information for tailoring the mold's microstructure and improving its mechanical properties. This review presents a unique perspective on the microstructure evolution in 3D printed steel molds. The microstructure evolution is discussed according to two major processing stages. Stage 1 describes the formation of the mold's microstructure in as-built condition after it has solidified from its molten state. Subsequently, Stage 2 describes the changes in the mold's microstructure post-heat treatment. This review also summarizes the various experimental techniques and numerical models used to study the microstructure evolution in 3D printed components. Advances in experimental microstructure characterization techniques enable researchers to investigate microstructure evolution in situ during metal AM processes. Coupled thermal-microstructure numerical models serve as an alternative approach for predicting grain growth in 3D printed components. The review concludes by summarizing future prospects in mold making and metal AM research in general.

Keywords additive manufacturing, injection molding, microstructure evolution, mold, steel

1. Introduction

Metal additive manufacturing (AM) technologies have risen in popularity due to its capability to produce fully functional components as well as process a growing selection of metals. The two main categories of metal AM technologies are: powder bed fusion (PBF) and directed energy deposition

(DED). Further distinction can be made for PBF category depending on the type of heat source used. Selective laser melting (SLM) utilizes a laser beam to melt and fuse powder material, while electron beam melting (EBM) utilizes an electron beam to achieve the same objective. Steel, titanium and nickel alloys are the most frequently studied materials in metal AM due to their widespread application in various industries. A review by Frazier (Ref 1) provided a broad perspective on the potential of various metal AM technologies. Also highlighted in the review are the advantages of using AM technologies as compared to conventional manufacturing processes.

Currently, the main challenge in metal AM research is to fabricate fully functional components with mechanical properties that are comparable to those produced by conventional manufacturing processes. The main issue with 3D printed components is they are unable to achieve full density due to the presence of defects in the microstructure. A review by Zhang et al. (Ref 2) described the formation mechanisms for the three most common microstructural defects in 3D printed components, which are: pores, cracks and incomplete fusion of powder material. These defects negatively impact the mechanical properties of 3D printed components, resulting in their inferior performance as compared to conventionally made ones. Another review by Zhang et al. (Ref 3) compared the achievable mechanical properties of 3D printed components and highlighted the need for an optimized solution to solve the problem of microstructural defects. This involves a deeper investigation on microstructure evolution in metal AM processes, and how does the microstructure of 3D printed components influence its mechanical properties.

In the injection molding industry, mold makers have explored using metal AM technologies to 3D print steel molds.

This invited article is part of a special topical focus in the *Journal of Materials Engineering and Performance* on Additive Manufacturing. The issue was organized by Dr. William Frazier, Pilgrim Consulting, LLC; Mr. Rick Russell, NASA; Dr. Yan Lu, NIST; Dr. Brandon D. Ribic, America Makes; and Caroline Vail, NSWC Carderock.

Wee King Law, Neutron Scattering Technical Engineering Research Center, School of Mechanical Engineering, Dongguan University of Technology, Dongguan 523808, China; and Department of Mechanical, Materials and Manufacturing Engineering, Faculty of Science and Engineering, University of Nottingham Malaysia, 43500 Semenyih, Selangor Darul Ehsan, Malaysia; **Kok-Cheong Wong** and **Chin Seong Lim**, Department of Mechanical, Materials and Manufacturing Engineering, Faculty of Science and Engineering, University of Nottingham Malaysia, 43500 Semenyih, Selangor Darul Ehsan, Malaysia; and **Haoliang Wang** and **Zhenzhong Sun**, Neutron Scattering Technical Engineering Research Center, School of Mechanical Engineering, Dongguan University of Technology, Dongguan 523808, China. Contact e-mails: kedy2lwg@nottingham.edu.my, kok-cheong.wong@nottingham.edu.my, hlwang@dgut.edu.cn, sunzz@dgut.edu.cn, and chinseong.lim@nottingham.edu.my.

Typical grades of steel mold materials include H13, AISI 420 stainless steel and 18Ni-300 maraging steel. Steel mold materials are chosen based on their achievable mechanical properties and microstructure characteristics. However, microstructural defects such as pores and cracks were also found in 3D printed steel molds.

The scope of this review focuses on the discussion of microstructure evolution in 3D printed steel molds. Steel mold materials are introduced, followed by the advantages of using metal AM technologies in mold making. The conventional and in situ microstructure characterization techniques used in metal AM research are then presented. The discussion on microstructure evolution in 3D printed steel molds is split into two main processing stages. Stage 1 focuses on the formation of the mold's microstructure as it solidifies into the as-built condition. Stage 2 focuses on changes in the mold's microstructure after subjecting it to post-heat treatment. Numerical modeling of microstructure evolution within the context of metal AM is then summarized. Finally, future prospects on the application of metal AM technologies for mold making as well as metal AM research in general are summarized.

1.1 Steel Mold Materials

Injection molding is known as one of the main manufacturing processes for mass production of polymer products. The term 'steel mold' refers to the mold used in injection molding process, which is made of steel. The geometry, contour and even the surface finish of polymer products are directly replicated from the mold itself. Injection molded polymer products have a widespread application across various industries, such as automotive, medical and electronics (Ref 4).

Injection molding is also applied in the manufacturing of metal components. This manufacturing process is known as metal injection molding (MIM) and is suited for the mass production of small metal components with complex geometries (Ref 5-7). MIM shares several similarities with injection molding of polymer products, such as the injection molding equipment used, mold material used, as well as considerations for mold design (Ref 8). To infer, this means that metal AM technologies could be used to fabricate steel molds for application in MIM.

This review focuses on the following steel mold materials: H13, P20, S136, AISI 420 stainless steel and 18Ni-300 maraging steel. The steel mold materials are categorized according to their precipitate strengthening elements. 18Ni-300 maraging steel is precipitate-strengthened via Ni-based intermetallics, while the other four steel mold materials are precipitate-strengthened via carbides. The chemical composition of steel mold materials mentioned in this review is summarized in Table 1.

In terms of mechanical properties, molds are required to have high yield strength ranging between 1500 and 2000 MPa in the post-heat-treated condition. This enables the mold to withstand the thermal and mechanical stresses induced during injection molding (Ref 9). Molds are also required to have high surface hardness, ranging between 50 and 54 HRC in the post-heat-treated condition. This property is especially important for the production of transparent polymer products, as well as polymer products that require mirror surface finish. This is because any defect on the mold surface is directly replicated on the polymer product itself. Table 2 provides a comparison for

the mechanical properties of steel mold materials, categorized according to its processing condition.

In terms of microstructure characteristics, a homogeneous microstructure is desirable for 3D printed steel molds as it leads to isotropic mechanical properties. A homogeneous microstructure also means that there are less nonmetallic inclusions (e.g., sulfides and oxides) in the microstructure, leading to improved microcleanliness and better polishability (Ref 10). In conventional mold making, electroslag remelting was utilized to obtain a more homogeneous microstructure in molds (Ref 11).

1.2 Advantages of using Metal Additive Manufacturing (AM) Technologies in Mold Making

The main advantages of utilizing metal AM technologies to 3D print steel molds include flexibility in mold design and reduced development lead time. This means that mold makers are able to fabricate molds with complex geometries, as well as test multiple prototypes during the design stage. However, mold makers need to be aware of the characteristics and limitations of 3D printed components when designing molds. These characteristics and limitations are summarized in Table 3, tabulated according to the respective metal AM technology.

3D printed steel molds differ from conventionally made ones as they are able to incorporate conformal cooling channels directly in their design. These cooling channels are designed according to the profile of the injection molded product to provide more efficient cooling during injection molding. Park and Dang (Ref 12) identified that the cooling stage occupied a large portion of the injection molding cycle. It was concluded that the use of conformally cooled mold inserts resulted in a 23% reduction in cooling time as compared to mold inserts that were cooled via conventional drilled channels. Evens et al. (Ref 13) also mentioned that conformal cooling channels greatly improved the performance of 3D printed steel molds. A reduction of 70% in molding cycle time was reported and startup losses were minimized.

Furthermore, Park et al. (Ref 14) highlighted the importance of conformal cooling channel design to achieve higher cooling efficiency. A combination of analytical and numerical methods was applied to devise an optimal design taking into consideration the complex features of the molded product and cooling channel geometry. Kanbur et al. (Ref 15) provided an overview on designing and optimizing conformal cooling channels via computer-aided engineering (CAE) simulations. The two main components for CAE analysis are: thermal and mechanical. Thermal analysis focuses on characterizing the performance of cooling channel geometries in terms of its surface temperature and coolant flow rate. Mechanical analysis includes the Von Mises stresses and fatigue life of molds.

2. Microstructure Characterization Techniques

Characterizing the microstructure of 3D printed components is an important step toward uncovering valuable insights on the process–microstructure–properties relationship in metal AM. The microstructure characterization techniques introduced in this review are categorized into two groups: conventional and in situ techniques. Conventional microstructure characterization techniques have been used extensively in material science to determine various aspects of the microstructure, such as grain

Table 1 Chemical composition of steel mold materials

Steel mold material	Chemical composition, wt.%													
	C	Cr	Ni	Mn	Mo	Si	V	Cu	Co	Ti	Al	P	S	Fe
H13 (Ref 16)	0.37	4.99	...	< 0.10	1.65	1.02	1.05	0.011	0.005	Balance
P20 (Ref 67)	0.40	1.95	...	0.83	0.33	0.45	...	0.02	Balance
AISI 420 stainless steel (Ref 72)	0.30	12.80	...	0.72	...	0.79	0.012	0.008	Balance
S136 (Ref 73)	0.29	13.55	...	0.98	...	0.96	0.4	0.010	...	Balance
18-Ni 300 maraging steel (Ref 86)	0.02	0.20	18.50	0.08	5.20	0.01	9.00	0.62	0.07	0.020	...	Balance

morphology, crystallographic texture, as well as the phases present in the material. On the other hand, in situ microstructure characterization techniques are relatively new, and it allows researchers to study microstructure evolution in real-time during metal AM processes.

2.1 Conventional Techniques: SEM, TEM, XRD

In metal AM research, conventional microstructure characterization techniques are used to examine the microstructure of a particular material before and after it is processed. Following that, a before–after comparison is made to deduce the microstructure evolution that occurred during the process. Conventional microstructure characterization techniques are further classified into two groups, which are: electron microscopy and x-ray diffraction (XRD). In electron microscopy, the two most commonly used techniques are: scanning electron microscopy (SEM) and transmission electron microscopy (TEM). Electron microscopy also features the following two complementary techniques, which are: energy-dispersive x-ray spectroscopy (EDS) and electron backscatter diffraction (EBSD). The EDS and EBSD results are often included in SEM and TEM analyses to obtain a thorough characterization of the microstructure.

A combination of several microstructure characterization techniques was applied to study the microstructure of 3D printed steel molds. For example, researchers have applied SEM and EDS to characterize the microstructure and chemical composition in 3D printed steel molds (Ref 16, 17). In addition, EBSD analysis was conducted to determine the crystallographic texture and grain size distribution in molds (Ref 18, 19). SEM, EDS and XRD were also used to identify the microstructure and phases present in molds (Ref 20–22).

2.2 In Situ Techniques: DTEM, Synchrotron X-Ray

Although conventional techniques possess the spatial resolution to characterize objects up to the nanometer scale, they lack the temporal resolution required to study and characterize the dynamics of microstructure evolution in situ. A before–after comparison of the microstructure obtained via conventional techniques is not sufficient to fully explain the evolution phenomenon that occurred during the process.

Thus, a new microstructure characterization technique termed dynamic transmission electron microscopy (DTEM) was developed to solve the problem of temporal resolution (Ref 23). DTEM enables researchers to observe and study transient phenomenon such as rapid solidification of alloys in situ, with both spatial and temporal resolutions up to the nanometer and

nanosecond scale, respectively. This was achieved by redesigning a conventional TEM to emit a large number of electrons in a short pulse, thus enabling transient phenomenon to be captured in real-time. Two derivative techniques were devised from DTEM, which are: single-shot mode and movie mode.

A review by McKeown et al. (Ref 24) explained the working principles of single-shot mode and movie mode DTEM. Single-shot mode DTEM involves taking an image of the evolution phenomenon at fixed time delays. By analyzing these images in sequence, new insights on microstructure evolution can be obtained. Movie mode DTEM improves on single-shot mode as it can capture images at user-defined time delays. This was achieved by controlling the time intervals for the emission of electron pulses, resulting in enhanced temporal control during data collection. Recent findings have reported the successful application of single-shot mode (Ref 25) and movie mode DTEM (Ref 26, 27) to study microstructure evolution in situ. McKeown et al. (Ref 27) utilized movie mode DTEM to study rapid solidification of hypoeutectic Al-Cu and Al-Si thin films (Fig. 1). A pulsed laser was used to induce rapid solidification in the samples, and the results obtained were used to determine the solidification front velocities of both alloys.

Besides DTEM, researchers also applied synchrotron x-ray techniques to study and capture microstructure evolution in situ. Synchrotron x-ray is produced from high energy electrons which are accelerated via a synchrotron machine (Ref 28). When the direction of electrons moving at high speed is altered, the electrons emit energy at x-ray wavelengths. This x-ray is then used to study microstructure evolution in situ during metal AM processes. Ultrafast in situ synchrotron x-ray imaging and diffraction techniques were developed by researchers to study the complex interaction between the heat source and the material (Ref 29). It was reported by Sun et al. (Ref 30) that this imaging technique has a minimum spatial resolution of 1 μm and a minimum temporal resolution of 100 ps.

Synchrotron x-ray techniques were successfully implemented for in situ investigations on pore formation mechanisms and melt pool dynamics in metal AM processes (Ref 31–38). Hojjatzadeh et al. (Ref 38) investigated the dynamics of pore motion within the melt pool using in situ synchrotron x-ray imaging. Figure 2 shows the formation of pores during PBF process captured using synchrotron x-ray imaging. It was identified that the movement of pores in the currently scanned region was governed by the thermocapillary force in the melt pool. This thermocapillary force was created as a result of the high thermal gradient between the heat source and melt pool

Table 2 A comparison for the mechanical properties of steel mold materials processed via conventional and metal AM technologies

Steel material	Manufacturing process	Condition	Young's modulus, GPa	Proof strength, MPa	0.2% Yield strength, MPa	Yield strength, MPa	Ultimate tensile strength, MPa	Elongation at fracture, %	Hardness (HV or HRC)
H13	Conventional (Ref 60, 131)	Heat-treated to 50 HRC	210	1596	1930	12.0	505 HV (50 HRC)
	Selective laser melting (SLM) (Ref 60, 62)	As-built, base plate preheated to 400°C Stress relieved (650°C/8h), hot isostatic pressed, hardened, and tempered (585°C/3h) (SR, HIP and HT)	194 191	1073 1502	1965 1743	3.7 6.6	667 HV 562 HV
P20	Conventional (Ref 132)	Forged, hardened and tempered to 34 HRC	205	896	1030	15.0	320 HV (34 HRC)
	SLM (Ref 67)	As-built	440–480 HV
	Conventional (Ref 54)	Pre-hardened	214.5	890	1100	9.0	320–340 HV
	SLM (Ref 72)	Heat-treated	...	1540	1940	15.0	53 HRC
		As-built	190	700	1050	2.5	55 HRC
		Tempered (315°C/.2h) and air quenched	195	950	1520	6.3	53 HRC
S136	Conventional (Ref 73)	Casted	41 HRC
	SLM (Ref 21, 74)	As-built (chemical composition #2, horizontal orientation)	–	1184.2	9.2	50 HRC
		As-built (chemical composition #2, vertical orientation)	1467.9	11.1	49 HRC
		Austenitized (1050°C/1h) and oil quenched	54 HRC
18-Ni 300 maraging steel	Conventional (Ref 77)	Wrought and aged	180	760–895	1000–1170	6.0–15.0	35 HRC
	SLM (Ref 79)	As-built	190	1910–2020	1951–2041	11.0	54 HRC
		Solution treated (840°C/1h) and aged (490°C/6h) (SAT)	915	1165	12.4	35–36 HRC
			1882	1943	5.6	52–54 HRC

Table 3 Characteristics and limitations of 3D printed components fabricated via metal AM technologies

Metal additive manufacturing (AM) technology	3D printed component					Limitations		
	Relative density, %	Surface finish of 3D printed component, $R_a(\mu m)$	Dimensional accuracy, mm	Maximal build envelope, mm^3	Minimum layer thickness, mm	Minimum feature size, mm	Minimum wall thickness, mm	Maximum component size, mm^3
Powder bed fusion (PBF)	Up to 99.9	4.0–10.0	$\pm 0.05 - 0.20$ ($\pm 0.1 - 0.2\%$)	$600 \times 400 \times 500$	0.03	0.04–0.20
Electron beam melting (EBM)	Up to 99.9	20.3–25.4 (Can be improved via post-processing)	± 0.20 (Can be improved via machining)	$350 \times 350 \times 380$	0.05	0.10
Directed energy deposition (DED)	...	25.4	0.25	0.75	$1500 \times 1500 \times 2100$

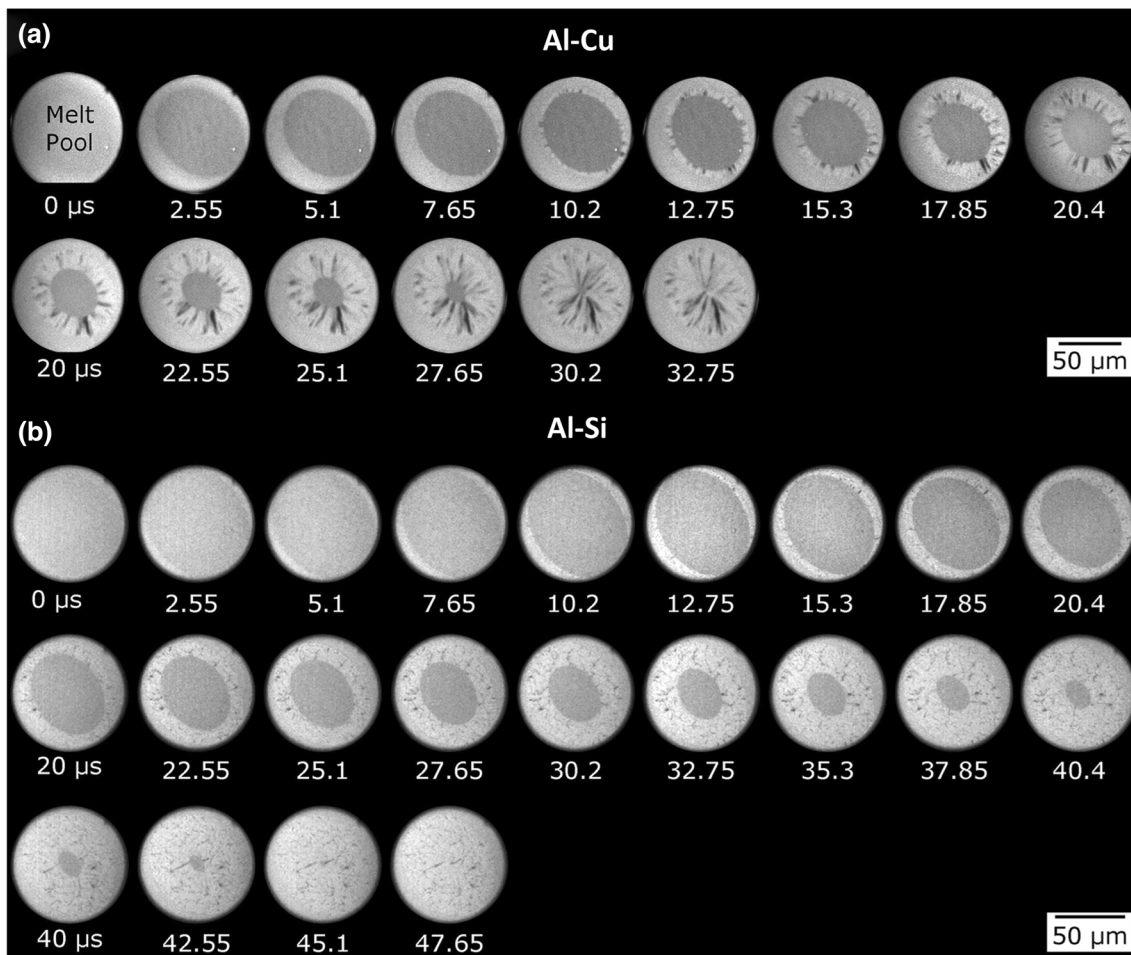


Fig. 1 Rapid solidification of (a) Al-Cu and (b) Al-Si thin films captured via movie mode DTEM. Reprinted by permission from Springer Nature Customer Service Centre GmbH: Springer Nature, *JOM*, Time-Resolved In Situ Measurements During Rapid Alloy Solidification: Experimental Insight for Additive Manufacturing, J.T. McKeown et al. (Ref 27) Copyright 2016, <https://link.springer.com/article/10.1007/s11837-015-1793-x>

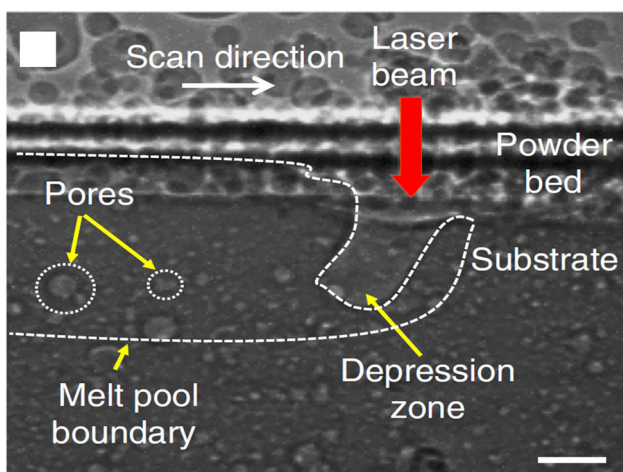


Fig. 2 Formation of pores during PBF process captured using synchrotron x-ray technique, the scale bar in the figure is 50 μm (Ref 38)

boundary. It was concluded that the thermocapillary force aided in pore elimination, as the pores escaped from the melt pool by traveling along the direction of thermal gradient.

3. Microstructure Evolution in Steel Molds Manufactured via Metal AM Processes

The mechanical properties of steel molds are directly influenced by the microstructure that forms at the end of the mold making process. The determining factors for the formation of a particular microstructure include the characteristics of powder material used to fabricate the mold, the process parameters used and the microstructure evolution that occurred during the process. By understanding the underlying physics which govern microstructure evolution in 3D printed steel molds, researchers are able to use this knowledge to optimize process parameters and fabricate steel molds with improved mechanical properties. Table 4 provides a comparison for the maximum relative density of 3D printed steel molds, along with the optimized process parameters used to fabricate it.

Currently, microstructural defects such as pores and cracks are found in 3D printed steel molds, as well as in other 3D printed components (Ref 39, 40). These defects create heterogeneity in the microstructure, resulting in inferior mechanical properties and reduced relative density. A review by Kok et al. (Ref 41) concluded that the anisotropy in mechanical properties and heterogeneity in the microstructure were influenced by

variations in grain morphology and crystallographic texture. Another review by Zhang et al. (Ref 42) explained how microstructure evolution phenomena such as grain growth and pore formation were influenced by metal AM process parameters such as energy density and scanning pattern. Also mentioned were the various strategies used to optimize metal AM process parameters.

Metal AM processes feature an interesting phenomenon known as intrinsic heat treatment (IHT). IHT can be understood as the effect of transient reheating on the adjacent regions of the current scan track (Ref 43–45). This effect is caused by the scanning movement of the heat source as it melts and solidifies the powder material. The heat from the melt pool is transferred toward its surroundings, causing a transient reheating effect on it. The effects of IHT in steel mold materials are illustrated in Fig. 3.

Metal AM processes also feature high cooling rates ranging between 10^3 and 10^6 K s⁻¹ (Ref 46, 47). In contrast, cooling rates obtained for conventional casting processes are much lower, ranging from 200 to 300 Ks⁻¹ (Ref 48). In terms of microstructure, finer grains are found in 3D printed components, while coarser grains are found in conventionally casted components. This is because the higher cooling rate in metal AM processes induced further grain refinement in the microstructure.

An article by Flemings (Ref 49) identified six different grain morphologies during the solidification process of directionally solidified alloys. Among them, the following three grain morphologies are commonly reported in 3D printed steel molds: equiaxed cellular grains, equiaxed dendrites and columnar dendrites. Figure 4 illustrates the relationship between thermal gradient and grain morphologies formed after rapid

Table 4 A comparison for the maximum relative density of 3D printed steel molds and the corresponding optimized process parameters used to fabricate it

Steel material	mold	Maximum relative density, %	Energy density, $E = \frac{P}{vht}$, J mm ⁻³	Optimized process parameters			
				Laser Power, P, W	Scanning Speed, v, mm s ⁻¹	Hatch spacing between scan tracks, h, mm	Layer thickness, t, mm
H13 (Ref 65)		99.20	106.25	170	400	0.10	0.04
P2 (Ref 67)		98.30	190.48	160	350	0.08	0.03
AISI 420 stain-less steel (Ref 70)		99.95	159.09	140	550	0.08	0.02
S136 (Ref 73)		98.90	58.33	280	800	0.12	0.05
18-Ni 300 maraging steel (Ref 86)		99.80	71.43	300	700	0.12	0.05

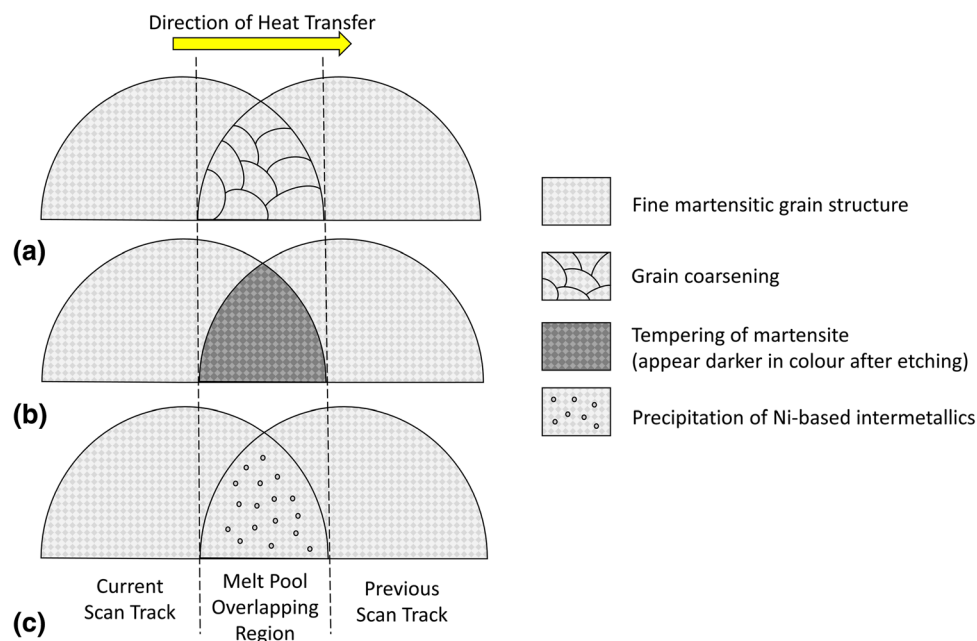


Fig. 3 Illustration for the effects of IHT in steel mold materials: (a) grain coarsening in melt pool overlapping regions; (b) tempering of martensite in carbide strengthened steel mold materials; and (c) precipitation of Ni-based intermetallics in maraging steel

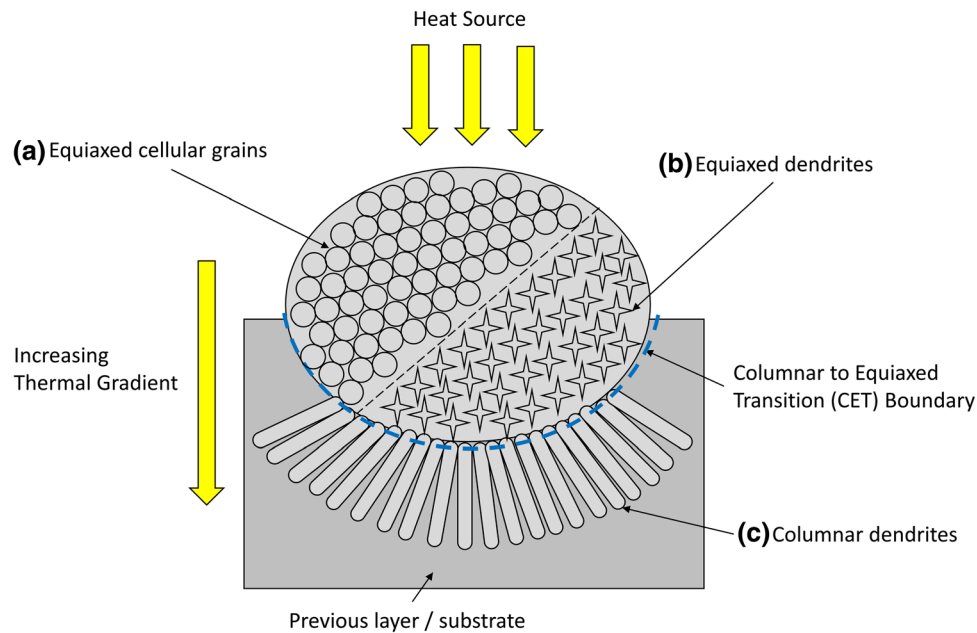


Fig. 4 Illustration for the formation of different grain morphologies after rapid solidification in metal AM processes: (a) equiaxed cellular grains, (b) equiaxed dendrites and (c) columnar dendrites

solidification in metal AM processes. During rapid solidification, columnar dendrites form in regions with a steep thermal gradient. The growth of columnar dendrites is oriented according to the direction of thermal gradient during solidification. In addition, the scanning movement of the heat source introduces a certain level of agitation on the melt pool. As a result, equiaxed cellular grains form in regions with vigorous agitation and low thermal gradient. Equiaxed cellular grains are replaced by equiaxed dendrites at lower agitation levels.

Similarities can be identified when comparing the solidification process and grain morphologies of 3D printed components to welded components. Schempp et al. (Ref 50) identified two important factors governing the formation of a particular grain morphology in welded components. The two factors were: the local thermal gradient between the heat source and melt pool boundary, and the solidification growth rate of the grains. Equiaxed grains were found in immediate regions that were scanned by the heat source, while columnar grains were found in regions that were further away from the heat source. In their subsequent work (Ref 51), they had deduced that the cooling rate obtained for welding process can be expressed as the product of the local thermal gradient and solidification growth rate. An expression for the critical thermal gradient where columnar to equiaxed transition (CET) occurs was also derived. A local thermal gradient that is less than the critical value resulted in the formation of equiaxed grains. The opposite, however, resulted in the formation of columnar grains. The presence of columnar grains was identified as the cause of anisotropy in mechanical properties, which is not desirable in welded components. This inference also applies to 3D printed components where anisotropy is regarded as detrimental to mechanical properties.

3.1 Steel Mold Materials Strengthened via Carbide Precipitation

The steel mold materials strengthened via carbide precipitation are further divided into two subgroups. The first subgroup consists of conventional steel mold materials, which are: H13 and P20. The second subgroup consists of steel mold materials with improved corrosion resistance, which are: AISI 420 stainless steel and S136. H13 and P20 are classified as conventional steel mold materials due to their extensive use in the mold making industry (Ref 52, 53). H13 is a type of hot work tool steel that is able to withstand thermal stresses at elevated temperatures while maintaining dimensional accuracy of the molded product. P20 is a type of low carbon tool steel commonly used in mold making, with characteristics such as good machinability and ease of repair via welding. AISI 420 stainless steel and its equivalent grade, S136 both possess improved corrosion resistance due to its high Cr content of up to 13.5 wt.%. It is suitable for injection molding of polymer products that require mirror surface finish and is able to process polymers such as polycarbonate (PC) and polyvinyl chloride (PVC) (Ref 54, 55).

3.1.1 Conventional Steel Mold Materials: H13 and P20. *3.1.1.1 Stage 1: As-Built Condition.* Several researchers have investigated the microstructure and mechanical properties of 3D printed H13 (Ref 16, 17, 56–66) and P20 (Ref 20, 67) samples. Deirmina et al. (Ref 64) reported the occurrence of IHT in 3D printed H13 samples. After etching, alternating rows of light and dark regions were observed in the microstructure (Fig. 5a). The light regions were identified to be untampered martensite, while the dark regions were identified as tempered martensite. It was deduced that in situ tempering of martensite phase had occurred in as-built condition. A higher magnification image of a heterogeneous distribution of cellular and columnar grains is shown in Fig. 5(b).

Mazumder et al. (Ref 57) identified that the microstructure of 3D printed H13 samples consisted of the following two grain

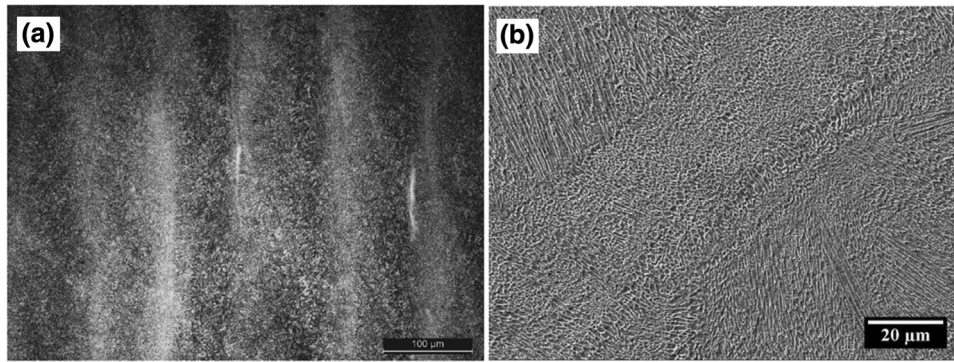


Fig. 5 Microstructure of 3D printed H13 samples in the as-built condition where (a) alternating rows of light and dark regions were observed. (b) A higher magnification image showing a heterogeneous microstructure. Reprinted from (Ref 64), Copyright 2019, with permission from Elsevier

morphologies: equiaxed dendrites and columnar dendrites. Equiaxed dendrites were found in immediate regions that were scanned by the heat source, and its growth was attributed to the uniform local thermal gradient in all directions. Columnar dendrites were found growing perpendicular to the region where equiaxed dendrites had formed. It was deduced that the growth of columnar dendrites was influenced by the direction of local thermal gradient during the solidification process.

Ren et al. (Ref 65) identified that the grain sizes found in 3D printed H13 samples were smaller compared to those found in conventionally forged samples. The presence of smaller grains was attributed to the influence of high cooling rate, which induced grain refinement in the microstructure. The phases found in 3D printed H13 samples were identified to be martensite and retained austenite. Carbide precipitates were found in conventionally forged samples, but were absent in 3D printed samples. It was deduced that the high cooling rate in metal AM processes had suppressed the diffusion and precipitation of carbides during the process. In terms of mechanical properties, the ultimate tensile strength and toughness obtained for 3D printed samples were slightly lower compared to conventionally forged samples. This was attributed to the lower relative density (99.2%) obtained for 3D printed samples as compared to conventionally forged ones.

Li et al. (Ref 67) investigated the microstructure of 3D printed P20 samples. The phases found in as-built condition consisted of mainly martensite with traces of retained austenite. The microstructure consisted of alternating rows of fine and coarse lath grains. The rows of fine grains were identified to be the scanning tracks where a higher energy intensity resulted in the formation of said grains. The rows of coarse grains were identified to be the melt pool overlapping regions where grain coarsening occurred.

3.1.1.2 Stage 2: Post-Heat Treatment Condition. Åsberg et al. (Ref 62) investigated the post-heat treatment effects on 3D printed H13 samples. The samples were subjected to the following heat treatment conditions: stress relief (SR) to reduce residual stress; hardening and tempering (HT) to improve hardness and strength; and hot isostatic pressing (HIP) to reduce porosity in the samples. It was reported that after SR, the martensite phase found in as-built condition decomposed into ferrite and carbide precipitates. The precipitates had formed a discontinuous network along prior austenite grain boundaries (Fig. 6a) and were rich in Cr and Mo. After HT, tempered martensite was found in the microstructure and carbides were

dispersed throughout the matrix. It was concluded that a combination of SR, HIP and HT led to reduced porosity, as well as improved hardness and strength in 3D printed H13 samples. Also, samples that had undergone SR, HIP, and HT have a more homogeneous microstructure as shown in Fig. 6(b).

Li et al. (Ref 67) investigated the effects of tempering on 3D printed P20 samples. Carbide precipitates were identified between martensite laths and consisted of mainly Cr and Si. As the tempering temperature was increased from 450 to 550 °C, the carbide precipitates grew larger and rounder in shape. An increase in corrosion resistance was observed in tempered P20 samples, while hardness remained similar to as-built condition.

3.1.2 Steel Mold Materials with Improved Corrosion Resistance: AISI 420 Stainless Steel and S136. **3.1.2.1 Stage 1: As-Built Condition.** Researchers have investigated using metal AM technologies to process AISI 420 stainless steel (Ref 18, 22, 68–72) and S136 (Ref 21, 73, 74). Sun et al. (Ref 71) observed a mix of columnar and cellular grains in 3D printed AISI 420 samples with continuous scan tracks. The phases found in as-built condition were identified as: ferrite, lath martensite and some regions of retained austenite. In addition, $M_{23}C_6$ carbides (M representing Fe and Cr) were found to be dispersed throughout the matrix. However, tempering was not observed in as-built samples with continuous scan tracks. When an idle time of 80 s was implemented between each scan track, tempered martensite was observed as dark bands in the melt pool overlapping regions. In addition, M_7C_3 carbides were found dispersed in the tempered martensite matrix. It was deduced that the idle time between scans allowed further cooling of the microstructure, while subsequent scans introduced in situ tempering. This resulted in the decomposition of martensite into ferrite and M_7C_3 carbide precipitates, indicated by a higher volume of carbide precipitation and dark bands of tempered martensite.

Wen et al. (Ref 73) investigated the microstructure of 3D printed S136 samples and compared it with conventionally casted samples. The microstructure in as-built samples consisted of finely distributed equiaxed and columnar grains, while coarse grains were found in conventionally casted samples. Phases identified in 3D printed samples consisted of mainly martensite with some retained austenite. No carbides were found in 3D printed samples. In contrast, conventionally casted samples contained fully martensite phase, and carbides rich in C and Cr were dispersed throughout the martensite matrix. The

variation in the results obtained was attributed to the large difference in cooling rate between the two processes.

3.1.2.2 Stage 2: Post-Heat Treatment Condition. Nath et al. (Ref 72) investigated the post-heat treatment effects on 3D printed AISI 420 samples. The samples were subjected to a tempering condition of 315 °C for 2 h. A relative density of over 99% was reported for as-built and tempered samples. A comparison of the microstructure found in as-built condition and after tempering is shown in Fig. 7. In Fig. 7(a), martensite laths were found to be dispersed in the microstructure of as-built samples. Tempering resulted in an increase in lath martensite, observed as needles with a darker shade in the microstructure as shown in Fig. 7(b). However, no carbides were found in as-built condition and after tempering. It was deduced that carbide precipitation may have been inhibited by rapid solidification during the process. Tempering also resulted in improved yield strength, ultimate tensile strength and ductility. However, no significant improvement in hardness and corrosion resistance was reported for tempered samples. After tempering, the mechanical properties of 3D printed samples were comparable with conventionally wrought samples.

Ji et al. (Ref 74) investigated the effects of manipulating the austenitizing temperature on 3D printed S136 samples. The samples were heated up to different austenitizing temperatures ranging from 980 to 1100 °C, and maintained for 1 h. The samples were then subjected to oil quenching. It was identified that the microstructure consisted of mainly martensite phase after quenching. In addition, carbides rich in C and Cr were found dispersed throughout the matrix. These carbides

appeared as white particles in samples that were austenitized at temperatures ranging between 980 and 1020 °C. However, no carbides were found when the austenitizing temperature was increased to 1100 °C. It was concluded that the carbides had dissolved in the matrix at higher austenitizing temperatures.

3.2 Steel Mold Materials Strengthened via Ni-based Intermetallics

3.2.1 18Ni-300 Maraging Steel. Maraging steel is a type of Fe-Ni alloy that is hardened via precipitation of Ni-based intermetallics. Its chemical composition consists of high Ni content (up to 19 wt.%), and very low C content (less than 0.03 wt.%). Conventionally, maraging steel was utilized in aerospace and tooling industries due to its superior strength and toughness (Ref 75). Recently, researchers have explored using maraging steel to 3D print molds. The grade of maraging steel commonly used to 3D print molds is 18Ni-300.

3.2.1.1 Stage 1: As-Built Condition. Researchers have conducted investigations on the microstructure of 3D printed maraging steel samples (Ref 19, 44, 76–79). Tan et al. (Ref 79) reported the microstructure of 3D printed maraging steel samples consisted of fine, equiaxed cellular grains in immediate regions scanned by the heat source (Fig. 8a). Equiaxed cellular grains were found in that region because the interfacial energies and grain boundary angles were in equilibrium, resulting in a stable crystalline structure. Coarse cellular grains were found in melt pool overlapping regions, indicating the effects of IHT during the process. In addition, columnar dendrites were found in areas further away from the scan track. The growth of

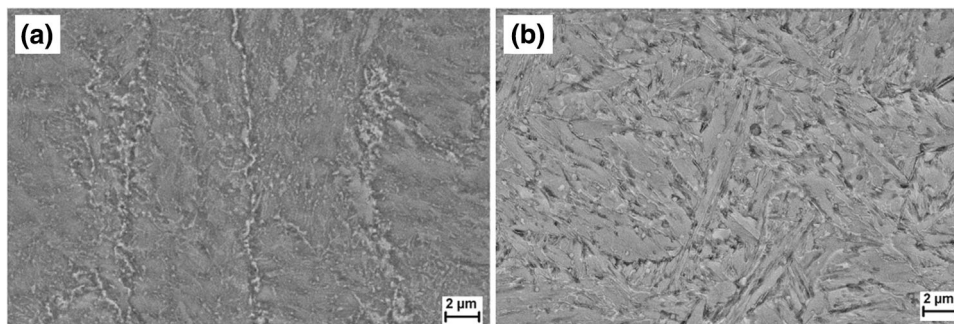


Fig. 6 Microstructure of 3D printed H13 samples after undergoing (a) SR and (b) a combination of SR, HIP and HT. Reprinted from (Ref 62), Copyright 2019, with permission from Elsevier

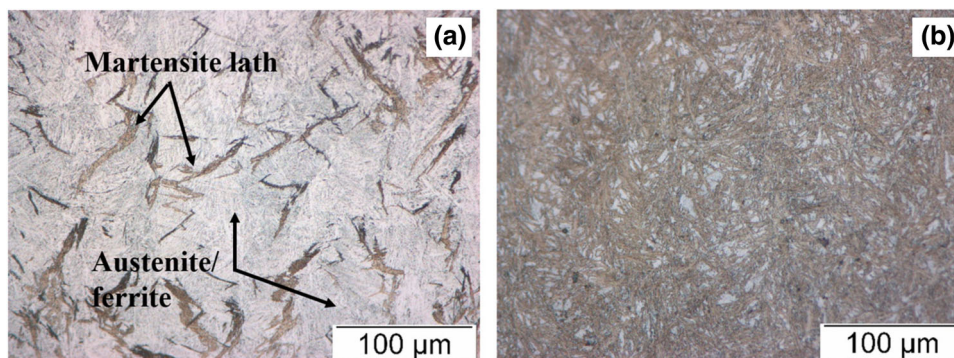


Fig. 7 Microstructure of 3D printed AISI 420 samples in the (a) as-built condition and (b) after tempering. Reprinted from (Ref 72), Copyright 2019, with permission from Elsevier

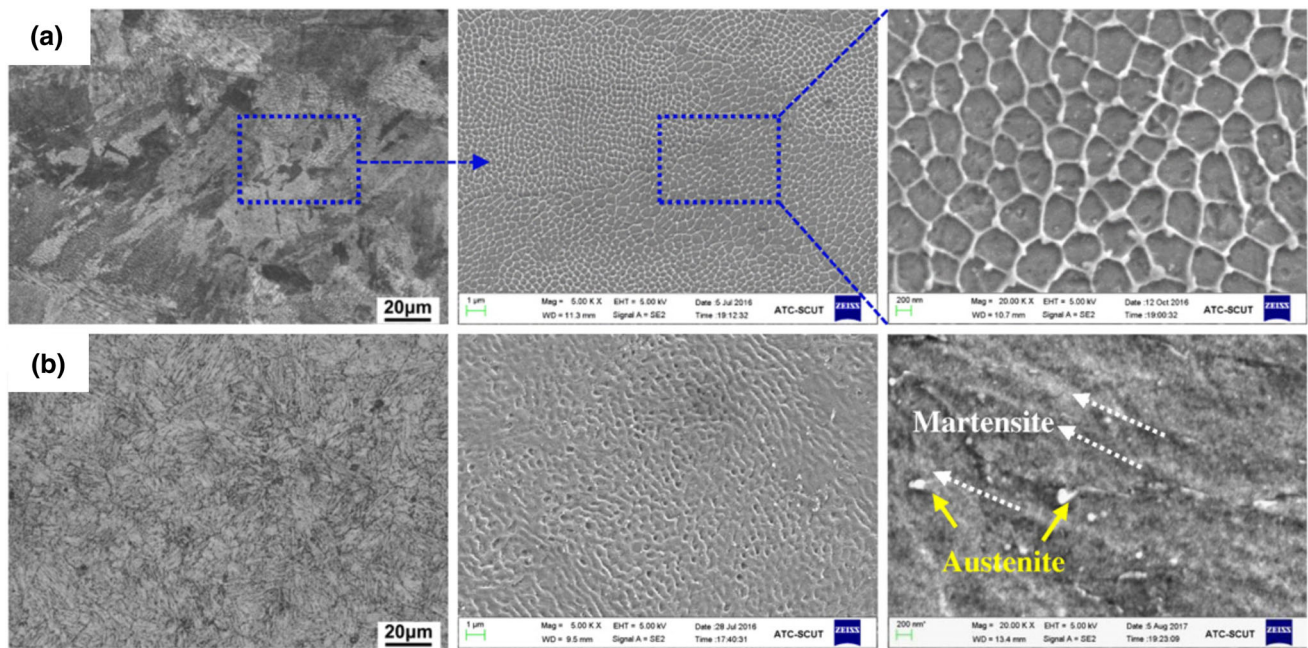


Fig. 8 Microstructure of 3D printed 18Ni-300 maraging steel samples in the (a) as-built condition and (b) after SAT. Reprinted from (Ref 79), Copyright 2017, with permission from Elsevier

columnar dendrites was influenced by the direction of local thermal gradient during the process. The microstructure in as-built samples consisted of mainly martensite phase with traces of retained austenite. It was deduced that the high cooling rate in metal AM processes favored the formation of martensite phase.

Investigations on the relationship between process parameters and mechanical properties of 3D printed maraging steel samples were also conducted (Ref 80–86). Mutua et al. (Ref 86) succeeded in 3D printing maraging steel samples with a maximum relative density of 99.8% using an optimized set of process parameters. It was concluded that less pores were found in samples with higher relative density. In addition, the building direction was found to influence the mechanical properties of 3D printed samples. Samples that were built perpendicular to the loading direction have higher ultimate tensile strength and improved ductility as compared to samples that were built parallel to the loading direction.

3.2.1.2 Stage 2: Post-Heat Treatment Condition. Researchers have conducted studies to investigate the effects of post-heat treatment in 3D printed maraging steel samples (Ref 87–94). Yin et al. (Ref 94) reported that the cellular structure found in as-built condition was no longer maintained after aging at 490 °C. Precipitation of Ni-based intermetallics was identified in aged samples. Ni_3Mo was identified to form first due to its lattice compatibility with martensite. Ni_3Ti was identified to form rapidly during aging due to the increased interaction between Ni and Ti. Ni_3Al formed as a result of Al replacing the remaining Ti in the matrix. Further aging at 590 °C resulted in the decomposition of Ni_3Mo and the formation of Fe_2Mo instead. Austenite reversion was identified in samples that were subjected to aging at 590 °C.

Tan et al. (Ref 79) reported that solution aging treatment (SAT) have improved the ultimate tensile strength, yield strength and hardness of 3D printed maraging steel samples. SAT involves solution treating the samples at 840 °C for 1 h,

followed by aging at 490 °C for 6 h. A comparison of the microstructure found in as-built condition and after SAT is shown in Fig. 8. The cellular shaped structure found in as-built condition (Fig. 8a) was no longer maintained, and was replaced with martensite laths (Fig. 8b). Austenite reversion was identified as white spots in the microstructure of SAT samples.

4. Numerical Modeling of Microstructure Evolution in Metal AM

Numerical modeling is also applied in metal AM research to predict microstructure evolution phenomena such as phase transformation and grain growth. The three main numerical models used to study microstructure evolution are: phase-field (PF), cellular automaton (CA) and kinetic Monte Carlo (MC). The underlying theories and capabilities of these three microstructure models were reviewed (Ref 95, 96). In order to study microstructure evolution in detail, a coupled thermal-microstructure numerical model is necessary. This involves the coupling of finite element (FE) or computational fluid dynamics (CFD) models with the aforementioned microstructure models to obtain an accurate prediction of microstructure evolution. This is because the thermal models provide essential thermodynamic information to predict the microstructure evolution in situ. Examples of the thermodynamic information provided include temperature profile, melt pool geometry, deformation characteristics and residual stress distribution.

Among the three microstructure models used to predict microstructure evolution, PF is known to give the highest resolution and is able to provide a microscale perspective on the phenomenon studied. PF is particularly useful for modeling microstructure evolution phenomena such as microsegregation of alloying elements (Ref 97, 98), precipitation kinetics (Ref 99, 100) and dendrite growth (Ref 101, 102). In PF, a diffuse

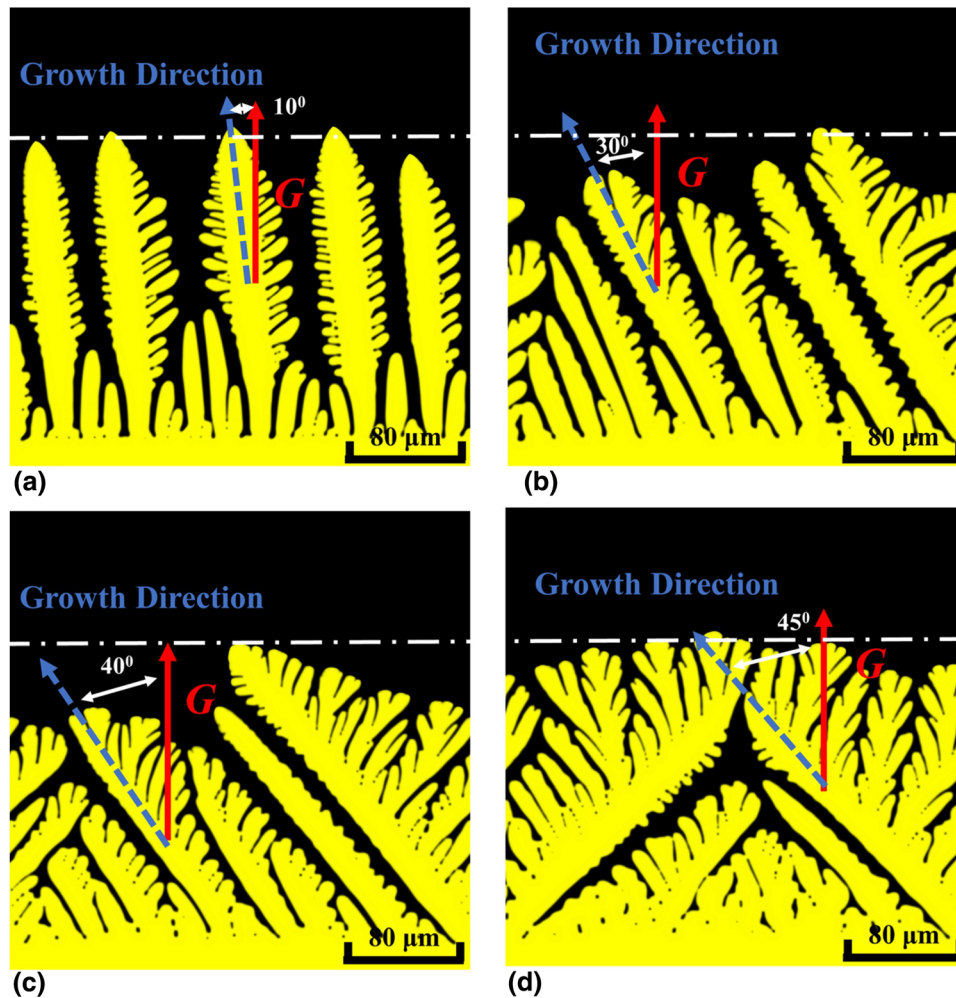


Fig. 9 Simulation of different dendrite growth angles ranging from (a) 10° to (d) 45° during the solidification of 3D printed IN718 alloy. The red solid arrow represents direction of thermal gradient G , while the blue dashed arrow represents the growth direction of primary dendrites. Reprinted by permission from Springer Nature Customer Service Centre GmbH: Springer Nature, *Journal of Materials Engineering and Performance*, Investigation on Microsegregation of IN718 Alloy During Additive Manufacturing via Integrated Phase-Field and Finite-Element Modeling, X. Wang et al., (Ref 101) Copyright 2018

interface approach is utilized to model the interface boundaries between different phases so that it varies continuously from one phase to another. However, PF is computationally intensive as it involves the use of thermodynamic databases.

CA differs from PF as it is more focused on mesoscale predictions, and is able to provide insights on how the mechanical properties of a certain material are related to the formation and structure of its grains. CA uses a mesh of equally divided cells to model the phenomenon of interest, and features explicit tracking of interface boundaries (Ref 103). Mesh dependency of CA is circumvented via the use of decentered square models, enabling a less restrictive prediction for the evolution phenomenon studied (Ref 104, 105).

Kinetic MC serves a similar purpose as CA in providing mesoscale predictions on microstructure evolution. In kinetic MC, each lattice site is assigned with an integer value for its orientation (Ref 106). The total energy of the system depends on the orientation of that lattice site in comparison to its neighboring sites. Neighboring sites with a different orientation will contribute to the total energy of the system, while neighboring sites with the same orientation do not. However, MC is unable to predict finer details of the microstructure such

as dendrite morphology. This is because the probabilistic methods used in MC lack the underlying physics to fully describe the evolution phenomenon (Ref 42).

Coupled thermal-microstructure numerical models have been applied to study microstructure evolution in 3D printed alloys. Several reviews were conducted on this topic (Ref 107–112). The following two alloys were frequently studied: Ti6Al4V titanium alloy (Ref 113–118) and IN718 nickel alloy (Ref 119–123). The microstructure evolution phenomena of interest are CET and the grain growth characteristics in both alloys. For example, a coupled FE-PF numerical model was used to predict the dendrite growth angles during the solidification of 3D printed IN718 nickel alloy (Fig. 9).

State of the art in the validation of the numerical results was done by correlating them with experimental data obtained via DTEM (Ref 124, 125). Pinomaa et al. (Ref 125) have simulated the solidification microstructure of Al-Cu thin films using PF and compared it with time-resolved DTEM images. At a time step of 8 μs , the predicted grain morphology (size and shape) was found to be in good agreement with those observed in DTEM images. However, at a time step of 11 μs , the predicted grain morphology was found to be larger when compared with

experimental data. It was mentioned that the predictions could be improved via the inclusion of latent heat effects, which would reduce the advance of the predicted solid–liquid interface.

Researchers have also reported the implementation of coupled thermal-microstructure numerical models to study steels (Ref 126–130). For example, Chen (Ref 130) implemented a coupled numerical model to simulate the grain morphologies formed after rapid solidification in 3D printed 304L stainless steel. The coupled numerical model consisted of three components: a FE model for generating the transient temperature profiles during rapid solidification; a Gibbs nucleation model incorporating the necessary parameters to predict grain nucleation and CET phenomenon; and a PF model to predict grain morphology and grain growth during the solidification process. It was reported that preliminary predictions for grain morphology were in close agreement with those observed experimentally. The predictions could be improved by using the same length scale for FE and PF models. This would result in a more accurate prediction for the local temperature profile and grain morphology.

However, simulation on the microstructure evolution in 3D printed steel molds remains relatively undiscovered. Given the recent success in microstructure modeling of other 3D printed alloys, it is highly suggestive that the models used could be adapted to study steel mold materials too. These studies would provide valuable information on the microstructure evolution of 3D printed steel molds and could be utilized to tailor the mold's microstructure and improve its mechanical properties.

5. Conclusion

To summarize, the optimization of process parameters is necessary for 3D printing steel molds with high relative density and improved mechanical properties. In situ investigations on microstructure evolution in 3D printed steel molds provide the required knowledge to achieve this objective. The formation of a homogeneous microstructure is favorable for 3D printed steel molds, as it leads to isotropic mechanical properties. Understanding the CET phenomenon in metal AM processes is crucial for obtaining the desired microstructure. Furthermore, the experimental techniques and numerical models presented in this review could be adapted to study CET phenomenon in 3D printed steel molds.

Metal AM technologies feature complex microstructure evolution phenomena such as rapid solidification and IHT. The microstructure and mechanical properties of 3D printed components were identified to be significantly different compared to those made via conventional manufacturing processes. Further investigation on the process–microstructure–properties relationship in metal AM has yielded important information on the underlying mechanisms governing microstructure evolution. This improved understanding could be applied to tailor the microstructure of 3D printed components. The development of in situ microstructure characterization techniques such as DTEM and synchrotron x-ray have enabled more detailed observation of transient phenomena such as rapid solidification and pore formation in metal AM processes. Coupled thermal-microstructure numerical models are recommended for enhanced prediction of microstructure evolution phenomena such as dendrite growth and CET in metal AM processes.

Acknowledgments

The authors express their gratitude for the financial support provided by the Joint Doctoral Training Programme established by Dongguan University of Technology in collaboration with University of Nottingham Malaysia.

References

1. W.E. Frazier, Metal Additive Manufacturing: A Review, *J. Mater. Eng. Perform.*, 2014, **23**(6), p 1917–1928. <https://doi.org/10.1007/s11665-014-0958-z>
2. B. Zhang, Y. Li and Q. Bai, Defect Formation Mechanisms in Selective Laser Melting: A Review, *Chin. J. Mech. Eng.*, 2017, **30**(3), p 515–527. <https://doi.org/10.1007/s10033-017-0121-5>
3. Y. Zhang, L. Wu, X. Guo, S. Kane, Y. Deng, Y.-G. Jung, J.-H. Lee and J. Zhang, Additive Manufacturing of Metallic Materials: A Review, *J. Mater. Eng. Perform.*, 2018, **27**(1), p 1–13. <https://doi.org/10.1007/s11665-017-2747-y>
4. Midstate Mold, Everyday Items Made in the Plastic Injection Molding Process, 2017 <https://www.midstatemold.com/everyday-items-plastic-injection/>. Accessed from 9 Dec 2020
5. CustomPart, “Metal Injection Molding (MIM),” n.d., <https://www.ustompartnet.com/wu/metal-injection-molding>. Accessed from 29 Apr 2021
6. Powder Injection Moulding (PIM) International, “Metal Injection Molding: An Introduction,” n.d., <https://www.pim-international.com/metal-injection-molding/metal-injection-moulding-introduction/>. Accessed from 29 Apr 2021
7. Metal Powder Products (MPP), “Metal Injection Molding (MIM),” n.d., <https://mppinnovation.com/metal-injection-molding/>. Accessed from 29 Apr 2021
8. Smith Metal Products, “Metal Injection Molding (MIM) Process Options - Tooling for MIM,” n.d., <https://smithmetals.com/design-guide/process-options/tooling-for-mim/>. Accessed from 29 Apr 2021
9. G. Roberts, G. Krauss, and R. Kennedy, Mold Steels, *Tool Steels*, 5th ed. ASM International, Ohio, 1998, p 291–292
10. J. Kaszynski, “What Do YOU Know About Mold Steel Quality?,” *MoldMaking Technology*, 2000, <https://www.moldmakingtechnology.com/articles/what-do-you-know-about-mold-steel-quality>. Accessed from 9 Dec 2020
11. X. Wang, G. Li, Y. Liu, Y. Cao, F. Wang and Q. Wang, Investigation of Primary Carbides in a Commercial-Sized Electroslag Remelting Ingot of H13 Steel, *Metals (Basel)*, 2019, **9**(12), p 1247. <https://doi.org/10.3390/met9121247>
12. H.-S. Park and X.-P. Dang, Development of a Smart Plastic Injection Mold with Conformal Cooling Channels, *Procedia Manuf.*, 2017, **10**, p 48–59. <https://doi.org/10.1016/j.promfg.2017.07.020>
13. T. Evens, W. Six, J. De Keyser, F. Desplentere, and A. Van Bael, Experimental Analysis of Conformal Cooling in SLM Produced Injection Moulds: Effects on Process and Product Quality. In: *AIP Conference Proceedings*, 2019, p 070017, <https://doi.org/10.1063/1.5084861>
14. H.-S. Park, X.-P. Dang, D.-S. Nguyen and S. Kumar, Design of Advanced Injection Mold to Increase Cooling Efficiency, *Int. J. Precis. Eng. Manuf. Technol.*, 2020, **7**(2), p 319–328. <https://doi.org/10.1007/s40684-019-00041-4>
15. B.B. Kanbur, S. Suping and F. Duan, Design and Optimization of Conformal Cooling Channels for Injection Molding: A Review, *Int. J. Adv. Manuf. Technol.*, 2020, **106**(7–8), p 3253–3271. <https://doi.org/10.1007/s00170-019-04697-9>
16. D. Cormier, O. Harrysson and H. West, Characterization of H13 Steel Produced via Electron Beam Melting, *Rapid Prototyp. J.*, 2004, **10**(1), p 35–41. <https://doi.org/10.1108/13552540410512516>
17. J. Choi and Y. Chang, Characteristics of Laser Aided Direct Metal/ Material Deposition Process for Tool Steel, *Int. J. Mach. Tools Manuf.*, 2005, **45**(4–5), p 597–607. <https://doi.org/10.1016/j.ijmachtools.2004.08.014>
18. M.K. Alam, M. Mehdi, R.J. Urbanic and A. Edrissy, Mechanical Behavior of Additive Manufactured AISI 420 Martensitic Stainless Steel, *Mater. Sci. Eng. A*, 2020, **773**, p 138815. <https://doi.org/10.1016/j.msea.2019.138815>

19. Y. Yao, K. Wang, X. Wang, L. Li, W. Cai, S. Kelly, N. Esparragoza, M. Rosser and F. Yan, Microstructural Heterogeneity and Mechanical Anisotropy of 18Ni-330 Maraging Steel Fabricated by Selective Laser Melting: The Effect of Build Orientation and Height, *J. Mater. Res.*, 2020, **35**(15), p 2065–2076. <https://doi.org/10.1557/jmr.2020.126>
20. J.-Y. Chen, K. Conlon, L. Xue and R. Rogge, Experimental Study of Residual Stresses in Laser Clad AISI P20 Tool Steel on Pre-Hardened Wrought P20 Substrate, *Mater. Sci. Eng. A*, 2010, **527**(27–28), p 7265–7273. <https://doi.org/10.1016/j.msea.2010.07.098>
21. Y. Zhou, L. Duan, X. Ji, S. Wen, Q. Wei, F. Ye and Y. Shi, Comparisons on Microstructure, Mechanical and Corrosion Resistant Property of S136 Mold Steel Processed by Selective Laser Melting from Two Pre-Alloy Powders with Trace Element Differences, *Opt. Laser Technol.*, 2018, **108**, p 81–89. <https://doi.org/10.1016/j.optlas.2018.06.057>
22. S.D. Nath, E. Clinning, G. Gupta, V. Wuelfrath-Poirier, G. L'Espérance, O. Gulsoy, M. Kearns and S.V. Atre, Effects of Nb and Mo on the Microstructure and Properties of 420 Stainless Steel Processed by Laser-Powder Bed Fusion, *Addit. Manuf.*, 2019, **28**, p 682–691. <https://doi.org/10.1016/j.addma.2019.06.016>
23. Lawrence Livermore National Laboratory, “Dynamic Transmission Electron Microscope (DTEM),” n.d., <https://pls.llnl.gov/resources/materials-science/dynamic-transmission-electron-microscope>. Accessed from 7 Dec 2020
24. J.T. McKeown, A.J. Clarke and J.M.K. Wiezorek, Imaging Transient Solidification Behavior, *MRS Bull.*, 2020, **45**(11), p 916–926. <https://doi.org/10.1557/mrs.2020.273>
25. T. LaGrange, M.R. Armstrong, K. Boyden, C.G. Brown, G.H. Campbell, J.D. Colvin, W.J. DeHope, A.M. Frank, D.J. Gibson, F.V. Hartemann, J.S. Kim, W.E. King, B.J. Pyke, B.W. Reed, M.D. Shirk, R.M. Shuttlesworth, B.C. Stuart, B.R. Torralva and N.D. Browning, Single-Shot Dynamic Transmission Electron Microscopy, *Appl. Phys. Lett.*, 2006, **89**(4), p 044105. <https://doi.org/10.1063/1.2236263>
26. T. LaGrange, B.W. Reed and D.J. Masiel, Movie-Mode Dynamic Electron Microscopy, *MRS Bull.*, 2015, **40**(1), p 22–28. <https://doi.org/10.1557/mrs.2014.282>
27. J.T. McKeown, K. Zwiack, C. Liu, D.R. Coughlin, A.J. Clarke, J.K. Baldwin, J.W. Gibbs, J.D. Roehling, S.D. Imhoff, P.J. Gibbs, D. Tourret, J.M.K. Wiezorek and G.H. Campbell, Time-Resolved In Situ Measurements During Rapid Alloy Solidification: Experimental Insight for Additive Manufacturing, *JOM*, 2016, **68**(3), p 985–999. <https://doi.org/10.1007/s11837-015-1793-x>
28. European Synchrotron Radiation Facility, “What Is a Synchrotron?,” n.d., <https://www.esrf.eu/about/synchrotron-science/synchrotron>. Accessed from 7 Dec 2020
29. Advanced Photon Source, “Imaging (XSD-IMG),” 2018, <https://www.aps.anl.gov/Imaging>. Accessed from 7 Dec 2020
30. T. Sun, W. Tan, L. Chen and A. Rollett, In Situ/Operando Synchrotron X-Ray Studies of Metal Additive Manufacturing, *MRS Bull.*, 2020, **45**(11), p 927–933. <https://doi.org/10.1557/mrs.2020.275>
31. R. Cunningham, C. Zhao, N. Parab, C. Kantzos, J. Pauza, K. Fezzaa, T. Sun and A.D. Rollett, Keyhole Threshold and Morphology in Laser Melting Revealed by Ultrahigh-Speed X-Ray Imaging, *Science*, 2019, **363**(6429), p 849–852. <https://doi.org/10.1126/science.aav4687>
32. N. Kourayem, X. Li, R. Cunningham, C. Zhao, N. Parab, T. Sun, A.D. Rollett, A.D. Spear and W. Tan, Effect of Laser-Matter Interaction on Molten Pool Flow and Keyhole Dynamics, *Phys. Rev. Appl.*, 2019, **11**(6), p 064054. <https://doi.org/10.1103/PhysRevApplied.11.064054>
33. N.D. Parab, C. Zhao, R. Cunningham, L.I. Escano, K. Fezzaa, W. Everhart, A.D. Rollett, L. Chen and T. Sun, Ultrafast X-Ray Imaging of Laser-Metal Additive Manufacturing Processes, *J. Synchrotron Radiat.*, 2018, **25**(5), p 1467–1477. <https://doi.org/10.1107/S1600577518009554>
34. A. Bobel, L.G. Hector, I. Chelladurai, A.K. Sachdev, T. Brown, W.A. Poling, R. Kubic, B. Gould, C. Zhao, N. Parab, A. Greco and T. Sun, In Situ Synchrotron X-Ray Imaging of 4140 Steel Laser Powder Bed Fusion, *Materialia*, 2019, **6**, p 100306. <https://doi.org/10.1016/j.mta.2019.100306>
35. S.A. Khairallah, A.T. Anderson, A. Rubenik and W.E. King, Laser Powder-Bed Fusion Additive Manufacturing: Physics of Complex Melt Flow and Formation Mechanisms of Pores Spatter, and Denudation Zones, *Acta Mater.*, 2016, **108**, p 36–45. <https://doi.org/10.1016/j.actamat.2016.02.014>
36. C. Zhao, K. Fezzaa, R.W. Cunningham, H. Wen, F. De. Carlo, L. Chen, A.D. Rollett and T. Sun, Real-Time Monitoring of Laser Powder Bed Fusion Process Using High-Speed X-Ray Imaging and Diffraction, *Sci. Rep.*, 2017, **7**(1), p 3602. <https://doi.org/10.1038/s41598-017-03761-2>
37. S.M.H. Hojjatzadeh, N.D. Parab, Q. Guo, M. Qu, L. Xiong, C. Zhao, L.I. Escano, K. Fezzaa, W. Everhart, T. Sun and L. Chen, Direct Observation of Pore Formation Mechanisms during LPBF Additive Manufacturing Process and High Energy Density Laser Welding, *Int. J. Mach. Tools Manuf.*, 2020, **153**, p 103555. <https://doi.org/10.1016/j.ijmactools.2020.103555>
38. S.M.H. Hojjatzadeh, N.D. Parab, W. Yan, Q. Guo, L. Xiong, C. Zhao, M. Qu, L.I. Escano, X. Xiao, K. Fezzaa, W. Everhart, T. Sun and L. Chen, Pore Elimination Mechanisms during 3D Printing of Metals, *Nat. Commun.*, 2019, **10**(1), p 3088. <https://doi.org/10.1038/s41467-019-10973-9>
39. N.T. Aboulkhair, N.M. Everitt, I. Ashcroft and C. Tuck, Reducing Porosity in AlSi10Mg Parts Processed by Selective Laser Melting, *Addit. Manuf.*, 2014, **1–4**, p 77–86. <https://doi.org/10.1016/j.addma.2014.08.001>
40. K. Kempen, L. Thijs, B. Vrancken, S. Buls, J. Van Humbeeck, and J.P. Kruth, “Producing Crack-Free, High Density M2 HSS Parts by Selective Laser Melting: Pre-Heating the Baseplate. In: *24th International SFF Symposium - An Additive Manufacturing Conference, SFF 2013*, 2013, p 131–139
41. Y. Kok, X.P. Tan, P. Wang, M.L.S. Nai, N.H. Loh, E. Liu and S.B. Tor, Anisotropy and Heterogeneity of Microstructure and Mechanical Properties in Metal Additive Manufacturing: A Critical Review, *Mater. Des.*, 2018, **139**, p 565–586. <https://doi.org/10.1016/j.matdes.2017.11.021>
42. X. Zhang, C.J. Yocom, B. Mao and Y. Liao, Microstructure Evolution during Selective Laser Melting of Metallic Materials: A Review, *J. Laser Appl.*, 2019, **31**(3), p 031201. <https://doi.org/10.2351/1.5085206>
43. E.V. Pereloma, A. Shekhter, M.K. Miller and S.P. Ringer, Ageing Behaviour of an Fe–20Ni–18Mn–16Ti–059Al Wt% Maraging Alloy: Clustering Precipitation and Hardening, *Acta Mater.*, 2004, **52**(19), p 5589–5602. <https://doi.org/10.1016/j.actamat.2004.08.018>
44. E.A. Jäggle, Z. Sheng, P. Kürnsteiner, S. Ocylok, A. Weisheit and D. Raabe, Comparison of Maraging Steel Micro- and Nanostructure Produced Conventionally and by Laser Additive Manufacturing, *Materials*, 2017, **10**(1), p 8. <https://doi.org/10.3390/ma10010008>
45. Y. Zhang, G. Yu and X. He, Numerical Study of Thermal History in Laser Aided Direct Metal Deposition Process, *Sci. China Phys. Mech. Astron.*, 2012, **55**(8), p 1431–1438. <https://doi.org/10.1007/s11433-012-4793-7>
46. M.H. Farshidianfar, A. Khajepour and A.P. Gerlich, Effect of Real-Time Cooling Rate on Microstructure in Laser Additive Manufacturing, *J. Mater. Process. Technol.*, 2016, **231**, p 468–478. <https://doi.org/10.1016/j.jmatprotec.2016.01.017>
47. P.A. Hooper, Melt Pool Temperature and Cooling Rates in Laser Powder Bed Fusion, *Addit. Manuf.*, 2018, **22**, p 548–559. <https://doi.org/10.1016/j.addma.2018.05.032>
48. S.W. Xu, K. Oh-ishi, S. Kamado, H. Takahashi and T. Homma, Effects of Different Cooling Rates during Two Casting Processes on the Microstructures and Mechanical Properties of Extruded Mg–Al–Ca–Mn Alloy, *Mater. Sci. Eng. A*, 2012, **542**, p 71–78. <https://doi.org/10.1016/j.msea.2012.02.034>
49. M.C. Flemings, Solidification Processing, *Materials Science and Technology*. Wiley-VCH Verlag GmbH & Co KGaA, Weinheim, Germany, 2006, p 4
50. P. Schempp, C. Cross, A. Pittner, G. Oder, R.S. Neumann, H. Rooch, I. Dörfel, W. Österle and M. Rethmeier, Solidification of GTA Aluminum Weld Metal: Part I - Grain Morphology Dependent upon Alloy Composition and Grain Refiner Content, *Weld. J.*, 2014, **93**, p 53s–59s
51. P. Schempp, C. Cross, A. Pittner and M. Rethmeier, Solidification of GTA Aluminum Weld Metal: Part 2 - Thermal Conditions and Model for Columnar-to-Equiaxed Transition, *Weld. J.*, 2014, **93**, p 69s–77s
52. Star Rapid, “How To Choose The Right Material For Plastic Injection Mold Tools,” n.d., <https://www.starrapid.com/blog/how-to-choose-the-right-material-for-plastic-injection-mold-tools/>. Accessed from 11 Dec 2020
53. ICOMold, “Injection Mold Materials,” n.d., <https://icomold.com/injection-mold-materials/>. Accessed from 11 Dec 2020

54. International Mold Steel, "S-Star 420 ESR Stainless Steel for Plastic Molds," *MatWeb*, n.d., <http://www.matweb.com/search/datasheet.aspx?matguid=1d44d407531c458799b92f3776bb651f>. Accessed from 9 Dec 2020
55. Otai Special Steel, "S136 Mold Steel," n.d., <https://www.otaisteel.com/s136-mold-steel/>. Accessed from 11 Dec 202
56. J. Mazumder, J. Choi, K. Nagarathnam, J. Koch and D. Hetzner, The Direct Metal Deposition of H13 Tool Steel for 3-D Components, *JOM*, 1997, **49**(5), p 55–60. <https://doi.org/10.1007/BF02914687>
57. J. Mazumder, A. Schifferer and J. Choi, Direct Materials Deposition: Designed Macro and Microstructure, *Mater. Res. Innov.*, 1999, **3**(3), p 118–131. <https://doi.org/10.1007/s100190050137>
58. G. Telasang, J. Dutta Majumdar, N. Wasekar, G. Padmanabham and I. Manna, Microstructure and Mechanical Properties of Laser Clad and Post-Cladding Tempered AISI H13 Tool Steel, *Metall. Mater. Trans. A*, 2015, **46**(5), p 2309–2321. <https://doi.org/10.1007/s11661-015-2757-z>
59. M. Lin, X. Zhao, L. Han, Q. Liu and J. Gu, Microstructural Evolution and Carbide Precipitation in a Heat-Treated H13 Hot Work Mold Steel, *Metallogr. Microstruct. Anal.*, 2016, **5**(6), p 520–527. <https://doi.org/10.1007/s13632-016-0318-5>
60. R. Mertens, B. Vrancken, N. Holmstock, Y. Kinds, J.-P. Kruth and J. Van Humbeeck, Influence of Powder Bed Preheating on Microstructure and Mechanical Properties of H13 Tool Steel SLM Parts, *Phys. Procedia*, 2016, **83**, p 882–890. <https://doi.org/10.1016/j.phpro.2016.08.092>
61. J. Šafka, M. Ackermann and L. Voleský, Structural Properties of H13 Tool Steel Parts Produced with Use of Selective Laser Melting Technology, *J. Phys. Conf. Ser.*, 2016, **709**, p 012004. <https://doi.org/10.1088/1742-6596/709/1/012004>
62. M. Åsberg, G. Fredriksson, S. Hatami, W. Fredriksson and P. Krakhmalev, Influence of Post Treatment on Microstructure, Porosity and Mechanical Properties of Additive Manufactured H13 Tool Steel, *Mater. Sci. Eng. A*, 2019, **742**, p 584–589. <https://doi.org/10.1016/j.msea.2018.08.046>
63. J.J. Yan, D.L. Zheng, H.X. Li, X. Jia, J.F. Sun, Y.L. Li, M. Qian and M. Yan, Selective Laser Melting of H13: Microstructure and Residual Stress, *J. Mater. Sci.*, 2017, **52**(20), p 12476–12485. <https://doi.org/10.1007/s10853-017-1380-3>
64. F. Deirmina, N. Peghini, B. AlMangour, D. Grzesiak and M. Pellizzari, Heat Treatment and Properties of a Hot Work Tool Steel Fabricated by Additive Manufacturing, *Mater. Sci. Eng. A*, 2019, **753**, p 109–121. <https://doi.org/10.1016/j.msea.2019.03.027>
65. B. Ren, D. Lu, R. Zhou, Z. Li and J. Guan, Preparation and Mechanical Properties of Selective Laser Melted H13 Steel, *J. Mater. Res.*, 2019, **34**(08), p 1415–1425. <https://doi.org/10.1557/jmr.2019.10>
66. Y. He, M. Zhong, J. Beuth and B. Webler, A Study of Microstructure and Cracking Behavior of H13 Tool Steel Produced by Laser Powder Bed Fusion Using Single-Tracks, Multi-Track Pads, and 3D Cubes, *J. Mater. Process. Technol.*, 2020, **286**, p 116802. <https://doi.org/10.1016/j.jmatprotec.2020.116802>
67. H.X. Li, H.L. Qi, C.H. Song, Y.L. Li and M. Yan, Selective Laser Melting of P20 Mould Steel: Investigation on the Resultant Microstructure, High-Temperature Hardness and Corrosion Resistance, *Powder Metall.*, 2018, **61**(1), p 21–27. <https://doi.org/10.1080/00325899.2017.1368965>
68. P. Krakhmalev, I. Yadroitsava, G. Fredriksson and I. Yadroitsev, In Situ Heat Treatment in Selective Laser Melted Martensitic AISI 420 Stainless Steels, *Mater. Des.*, 2015, **87**, p 380–385. <https://doi.org/10.1016/j.matdes.2015.08.045>
69. X. Zhao, B. Song, Y. Zhang, X. Zhu, Q. Wei and Y. Shi, Decarburization of Stainless Steel during Selective Laser Melting and Its Influence on Young's Modulus, Hardness and Tensile Strength, *Mater. Sci. Eng. A*, 2015, **647**, p 58–61. <https://doi.org/10.1016/j.msea.2015.08.061>
70. X. Zhao, Q. Wei, B. Song, Y. Liu, X. Luo, S. Wen and Y. Shi, Fabrication and Characterization of AISI 420 Stainless Steel Using Selective Laser Melting, *Mater. Manuf. Process.*, 2015, **30**(11), p 1283–1289. <https://doi.org/10.1080/10426914.2015.1026351>
71. S. Sun, D. Fabijanic, C. Barr, Q. Liu, K. Walker, N. Matthews, N. Orchowski, M. Easton and M. Brandt, In-Situ Quench and Tempering for Microstructure Control and Enhanced Mechanical Properties of Laser Cladded AISI 420 Stainless Steel Powder on 300M Steel Substrates, *Surf. Coat. Technol.*, 2018, **333**, p 210–219. <https://doi.org/10.1016/j.surfcoat.2017.10.080>
72. S.D. Nath, H. Irrinki, G. Gupta, M. Kearns, O. Gulsoy and S. Atre, Microstructure-Property Relationships of 420 Stainless Steel Fabricated by Laser-Powder Bed Fusion, *Powder Technol.*, 2019, **343**, p 738–746. <https://doi.org/10.1016/j.powtec.2018.11.075>
73. S.-F. Wen, X.-T. Ji, Y. Zhou, C.-J. Han, Q.-S. Wei and Y.-S. Shi, Corrosion Behavior of the S136 Mold Steel Fabricated by Selective Laser Melting, *Chin. J. Mech. Eng.*, 2018, **31**(1), p 108. <https://doi.org/10.1186/s10033-018-0312-8>
74. X. Ji, S. Wen, Q. Wei, Y. Zhou and Z. Chen, Effect of Quenching Treatment on Performance of S136 Steel Fabricated via Selective Laser Melting, *J. ZheJiang Univ. Eng. Sci.*, 2019, **53**(4), p 664–670. (in Chinese)
75. W. Sha and Z. Guo, What Are Maraging Steels?, *Maraging Steels: Modelling of Microstructure, Properties and Applications*, 1st ed. Woodhead Publishing, New Delhi, 2009, p 1–3
76. Y. Bai, Y. Yang, D. Wang and M. Zhang, Influence Mechanism of Parameters Process and Mechanical Properties Evolution Mechanism of Maraging Steel 300 by Selective Laser Melting, *Mater. Sci. Eng. A*, 2017, **703**, p 116–123. <https://doi.org/10.1016/j.msea.2017.06.033>
77. K. Kempen, E. Yasa, L. Thijs, J.-P. Kruth and J. Van Humbeeck, Microstructure and Mechanical Properties of Selective Laser Melted 18Ni-300 Steel, *Phys. Procedia*, 2011, **12**, p 255–263. <https://doi.org/10.1016/j.phpro.2011.03.033>
78. P. Kürnsteiner, M.B. Wilms, A. Weisheit, P. Barriobero-Vila, E.A. Jägler and D. Raabe, Massive Nanoprecipitation in an Fe-19Ni- x Al Maraging Steel Triggered by the Intrinsic Heat Treatment during Laser Metal Deposition, *Acta Mater.*, 2017, **129**, p 52–60. <https://doi.org/10.1016/j.actamat.2017.02.069>
79. C. Tan, K. Zhou, W. Ma, P. Zhang, M. Liu and T. Kuang, Microstructural Evolution, Nanoprecipitation Behavior and Mechanical Properties of Selective Laser Melted High-Performance Grade 300 Maraging Steel, *Mater. Des.*, 2017, **134**, p 23–34. <https://doi.org/10.1016/j.matdes.2017.08.026>
80. T. Herrmann Becker and D. Dimitrov, The Achievable Mechanical Properties of SLM Produced Maraging Steel 300 Components, *Rapid Prototyp. J.*, 2016, **22**(3), p 487–494. <https://doi.org/10.1108/RPJ-08-2014-0096>
81. G. Casalino, S.L. Campanelli, N. Contuzzi and A.D. Ludovico, Experimental Investigation and Statistical Optimisation of the Selective Laser Melting Process of a Maraging Steel, *Opt. Laser Technol.*, 2015, **65**, p 151–158. <https://doi.org/10.1016/j.optlastec.2014.07.021>
82. S.L. Campanelli, A. Angelastro, C.G. Signorile and G. Casalino, Investigation on Direct Laser Powder Deposition of 18 Ni (300) Marage Steel Using Mathematical Model and Experimental Characterisation, *Int. J. Adv. Manuf. Technol.*, 2017, **89**(1–4), p 885–895. <https://doi.org/10.1007/s00170-016-9135-x>
83. A.G. Demir and B. Previtali, Investigation of Remelting and Preheating in SLM of 18Ni300 Maraging Steel as Corrective and Preventive Measures for Porosity Reduction, *Int. J. Adv. Manuf. Technol.*, 2017, **93**(5–8), p 2697–2709. <https://doi.org/10.1007/s00170-017-0697-z>
84. L. Mugwagwa, I. Yadroitsev and S. Matope, Effect of Process Parameters on Residual Stresses, Distortions, and Porosity in Selective Laser Melting of Maraging Steel 300, *Metals*, 2019, **9**(10), p 1042. <https://doi.org/10.3390/met9101042>
85. T. Bhardwaj and M. Shukla, Effect of Laser Scanning Strategies on Texture, Physical and Mechanical Properties of Laser Sintered Maraging Steel, *Mater. Sci. Eng. A*, 2018, **734**, p 102–109. <https://doi.org/10.1016/j.msea.2018.07.089>
86. J. Mutua, S. Nakata, T. Onda and Z.-C. Chen, Optimization of Selective Laser Melting Parameters and Influence of Post Heat Treatment on Microstructure and Mechanical Properties of Maraging Steel, *Mater. Des.*, 2018, **139**, p 486–497. <https://doi.org/10.1016/j.matdes.2017.11.042>
87. S. Bodziak, K.S. Al-Rubaie, L.D. Valentina, F.H. Lafratta, E.C. Santos, A.M. Zanatta and Y. Chen, Precipitation in 300 Grade Maraging Steel Built by Selective Laser Melting: Aging at 510 °C for 2 H, *Mater. Charact.*, 2019, **151**, p 73–83. <https://doi.org/10.1016/j.matchar.2019.02.033>
88. R. Casati, J. Lemke, A. Tuissi and M. Vedani, Aging Behaviour and Mechanical Performance of 18-Ni 300 Steel Processed by Selective Laser Melting, *Metals (Basel)*, 2016, **6**(9), p 218. <https://doi.org/10.3390/met6090218>
89. R. Casati, J. Lemke and M. Vedani, Microstructural and Mechanical Properties of As Built, Solution Treated and Aged 18 Ni (300 Grade)

- Maraging Steel Produced by Selective Laser Melting, *Metall. Ital.*, 2017, **109**, p 11–20
90. Y. Bai, D. Wang, Y. Yang and H. Wang, Effect of Heat Treatment on the Microstructure and Mechanical Properties of Maraging Steel by Selective Laser Melting, *Mater. Sci. Eng. A*, 2019, **760**, p 105–117. <https://doi.org/10.1016/j.msea.2019.05.115>
 91. E.A. Jäggle, P.-P. Choi, J. Van Humbeeck and D. Raabe, Precipitation and Austenite Reversion Behavior of a Maraging Steel Produced by Selective Laser Melting, *J. Mater. Res.*, 2014, **29**(17), p 2072–2079. <https://doi.org/10.1557/jmr.2014.204>
 92. C. Tan, K. Zhou, M. Kuang, W. Ma and T. Kuang, Microstructural Characterization and Properties of Selective Laser Melted Maraging Steel with Different Build Directions, *Sci. Technol. Adv. Mater.*, 2018, **19**(1), p 746–758. <https://doi.org/10.1080/14686996.2018.1527645>
 93. B. Mooney, K.I. Kourousis and R. Raghavendra, Plastic Anisotropy of Additively Manufactured Maraging Steel: Influence of the Build Orientation and Heat Treatments, *Addit. Manuf.*, 2019, **25**, p 19–31. <https://doi.org/10.1016/j.addma.2018.10.032>
 94. S. Yin, C. Chen, X. Yan, X. Feng, R. Jenkins, P. O'Reilly, M. Liu, H. Li and R. Lupoi, The Influence of Aging Temperature and Aging Time on the Mechanical and Tribological Properties of Selective Laser Melted Maraging 18Ni-300 Steel, *Addit. Manuf.*, 2018, **22**, p 592–600. <https://doi.org/10.1016/j.addma.2018.06.005>
 95. J.H.K. Tan, S.L. Sing and W.Y. Yeong, Microstructure Modelling for Metallic Additive Manufacturing: A Review, *Virtual Phys. Prototyp.*, 2020, **15**(1), p 87–105. <https://doi.org/10.1080/17452759.2019.1677345>
 96. C. Körner, M. Markl and J.A. Koepf, Modeling and Simulation of Microstructure Evolution for Additive Manufacturing of Metals: A Critical Review, *Metall. Mater. Trans. A*, 2020, **51**(10), p 4970–4983. <https://doi.org/10.1007/s11661-020-05946-3>
 97. J.A. Warren and W.J. Boettinger, Prediction of Dendritic Growth and Microsegregation Patterns in a Binary Alloy Using the Phase-Field Method, *Acta Metall. Mater.*, 1995, **43**(2), p 689–703. [https://doi.org/10.1016/0956-7151\(94\)00285-P](https://doi.org/10.1016/0956-7151(94)00285-P)
 98. S. Ghosh, L. Ma, N. Ofori-Opoku and J.E. Guyer, On the Primary Spacing and Microsegregation of Cellular Dendrites in Laser Deposited Ni–Nb Alloys, *Model. Simul. Mater. Sci. Eng.*, 2017, **25**(6), p 065002. <https://doi.org/10.1088/1361-651X/aa7369>
 99. M. Fleck, F. Schleifer, M. Holzinger and U. Glatzel, Phase-Field Modeling of Precipitation Growth and Ripening During Industrial Heat Treatments in Ni-Base Superalloys, *Metall. Mater. Trans. A*, 2018, **49**(9), p 4146–4157. <https://doi.org/10.1007/s11661-018-4746-5>
 100. G. Han, Z. Han, A.A. Luo and B. Liu, Three-Dimensional Phase-Field Simulation and Experimental Validation of β -Mg17Al12 Phase Precipitation in Mg-Al-Based Alloys, *Metall. Mater. Trans. A*, 2015, **46**(2), p 948–962. <https://doi.org/10.1007/s11661-014-2674-6>
 101. X. Wang, P.W. Liu, Y. Ji, Y. Liu, M.H. Horstemeyer and L. Chen, Investigation on Microsegregation of IN718 Alloy During Additive Manufacturing via Integrated Phase-Field and Finite-Element Modeling, *J. Mater. Eng. Perform.*, 2019, **28**(2), p 657–665. <https://doi.org/10.1007/s11665-018-3620-3>
 102. T. Keller, G. Lindwall, S. Ghosh, L. Ma, B.M. Lane, F. Zhang, U.R. Kattner, E.A. Lass, J.C. Heigel, Y. Idell, M.E. Williams, A.J. Allen, J.E. Guyer and L.E. Levine, Application of Finite Element, Phase-Field, and CALPHAD-Based Methods to Additive Manufacturing of Ni-Based Superalloys, *Acta Mater.*, 2017, **139**, p 244–253. <https://doi.org/10.1016/j.actamat.2017.05.003>
 103. A. Choudhury, K. Reuther, E. Wesner, A. August, B. Nestler and M. Rettenmayr, Comparison of Phase-Field and Cellular Automaton Models for Dendritic Solidification in Al–Cu Alloy, *Comput. Mater. Sci.*, 2012, **55**, p 263–268. <https://doi.org/10.1016/j.commatsci.2011.12.019>
 104. C.-A. Gandin and M. Rappaz, A 3D Cellular Automaton Algorithm for the Prediction of Dendritic Grain Growth, *Acta Mater.*, 1997, **45**(5), p 2187–2195. [https://doi.org/10.1016/S1359-6454\(96\)00303-5](https://doi.org/10.1016/S1359-6454(96)00303-5)
 105. W. Wang, P.D. Lee and M. McLean, A Model of Solidification Microstructures in Nickel-Based Superalloys: Predicting Primary Dendrite Spacing Selection, *Acta Mater.*, 2003, **51**(10), p 2971–2987. [https://doi.org/10.1016/S1359-6454\(03\)00110-1](https://doi.org/10.1016/S1359-6454(03)00110-1)
 106. T.M. Rodgers, J.D. Madison and V. Tikare, Simulation of Metal Additive Manufacturing Microstructures Using Kinetic Monte Carlo, *Comput. Mater. Sci.*, 2017, **135**, p 78–89. <https://doi.org/10.1016/j.commatsci.2017.03.053>
 107. J. Li, X. Zhou, M. Brochu, N. Provas and Y.F. Zhao, Solidification Microstructure Simulation of Ti-6Al-4V in Metal Additive Manufacturing: A Review, *Addit. Manuf.*, 2020, **31**, p 100989. <https://doi.org/10.1016/j.addma.2019.100989>
 108. S. Ghosh, Predictive Modeling of Solidification during Laser Additive Manufacturing of Nickel Superalloys: Recent Developments, Future Directions, *Mater. Res. Express*, 2018, **5**(1), p 012001. <https://doi.org/10.1088/2053-1591/aaa04c>
 109. M.A. Miodownik, A Review of Microstructural Computer Models Used to Simulate Grain Growth and Recrystallisation in Aluminium Alloys, *J. Light Met.*, 2002, **2**(3), p 125–135. [https://doi.org/10.1016/S1471-5317\(02\)00039-1](https://doi.org/10.1016/S1471-5317(02)00039-1)
 110. K. Reuther and M. Rettenmayr, Perspectives for Cellular Automata for the Simulation of Dendritic Solidification – A Review, *Comput. Mater. Sci.*, 2014, **95**, p 213–220. <https://doi.org/10.1016/j.commatsci.2014.07.037>
 111. H. Zhu, F. Chen, H. Zhang and Z. Cui, Review on Modeling and Simulation of Microstructure Evolution during Dynamic Recrystallization Using Cellular Automaton Method, *Sci. China Technol. Sci.*, 2020, **63**(3), p 357–396. <https://doi.org/10.1007/s11431-019-9548-x>
 112. M. Militzer, Phase Field Modeling of Microstructure Evolution in Steels, *Curr. Opin. Solid State Mater. Sci.*, 2011, **15**(3), p 106–115. <https://doi.org/10.1016/j.cossms.2010.10.001>
 113. P.W. Liu, Y.Z. Ji, Z. Wang, C.L. Qiu, A.A. Antonysamy, L.-Q. Chen, X.Y. Cui and L. Chen, Investigation on Evolution Mechanisms of Site-Specific Grain Structures during Metal Additive Manufacturing, *J. Mater. Process. Technol.*, 2018, **257**, p 191–202. <https://doi.org/10.1016/j.jmatprotec.2018.02.042>
 114. P.W. Liu, Z. Wang, Y.H. Xiao, R.A. Lebensohn, Y.C. Liu, M.F. Horstemeyer, X.Y. Cui and L. Chen, Integration of Phase-Field Model and Crystal Plasticity for the Prediction of Process-Structure-Property Relation of Additively Manufactured Metallic Materials, *Int. J. Plast.*, 2020, **128**, p 102670. <https://doi.org/10.1016/j.ijplas.2020.102670>
 115. T. Pinomaa, I. Yashchuk, M. Lindroos, T. Andersson, N. Provas and A. Laukkanen, Process-Structure-Properties-Performance Modeling for Selective Laser Melting, *Metals (Basel)*, 2019, **9**(11), p 1138. <https://doi.org/10.3390/met9111138>
 116. J. Yang, H. Yu, H. Yang, F. Li, Z. Wang and X. Zeng, Prediction of Microstructure in Selective Laser Melted Ti 6Al 4V Alloy by Cellular Automaton, *J. Alloys Compd.*, 2018, **748**, p 281–290. <https://doi.org/10.1016/j.jallcom.2018.03.116>
 117. D. Liu and Y. Wang, Mesoscale Multi-Physics Simulation of Rapid Solidification of Ti-6Al-4V Alloy, *Addit. Manuf.*, 2019, **25**, p 551–562. <https://doi.org/10.1016/j.addma.2018.12.005>
 118. Z. Zhang, Z.J. Tan, X.X. Yao, C.P. Hu, P. Ge, Z.Y. Wan, J.Y. Li and Q. Wu, Numerical Methods for Microstructural Evolutions in Laser Additive Manufacturing, *Comput. Math. with Appl.*, 2019, **78**(7), p 2296–2307. <https://doi.org/10.1016/j.camwa.2018.07.011>
 119. R. Acharya, J.A. Sharon and A. Staroselsky, Prediction of Microstructure in Laser Powder Bed Fusion Process, *Acta Mater.*, 2017, **124**, p 360–371. <https://doi.org/10.1016/j.actamat.2016.11.018>
 120. J. Akram, P. Chalavadi, D. Pal and B. Stucker, Understanding Grain Evolution in Additive Manufacturing through Modeling, *Addit. Manuf.*, 2018, **21**, p 255–268. <https://doi.org/10.1016/j.addma.2018.03.021>
 121. X. Wang and K. Chou, Microstructure Simulations of Inconel 718 during Selective Laser Melting Using a Phase Field Model, *Int. J. Adv. Manuf. Technol.*, 2019, **100**(9–12), p 2147–2162. <https://doi.org/10.1007/s00170-018-2814-z>
 122. P. Liu, Z. Wang, Y. Xiao, M.F. Horstemeyer, X. Cui and L. Chen, Insight into the Mechanisms of Columnar to Equiaxed Grain Transition during Metallic Additive Manufacturing, *Addit. Manuf.*, 2019, **26**, p 22–29. <https://doi.org/10.1016/j.addma.2018.12.019>
 123. A. Rai, M. Markl and C. Körner, A Coupled Cellular Automaton-Lattice Boltzmann Model for Grain Structure Simulation during Additive Manufacturing, *Comput. Mater. Sci.*, 2016, **124**, p 37–48. <https://doi.org/10.1016/j.commatsci.2016.07.005>
 124. T. Pinomaa, A. Laukkanen and N. Provas, Solute Trapping in Rapid Solidification, *MRS Bull.*, 2020, **45**(11), p 910–915. <https://doi.org/10.1557/mrs.2020.274>
 125. T. Pinomaa, J.M. McKeown, J.M.K. Wieszorek, N. Provas, A. Laukkanen and T. Suhonen, Phase Field Modeling of Rapid Resolidification of Al-Cu Thin Films, *J. Cryst. Growth*, 2020, **532**, p 125418. <https://doi.org/10.1016/j.jcrysgro.2019.125418>

126. H. Yin and S.D. Felicelli, Dendrite Growth Simulation during Solidification in the LENS Process, *Acta Mater.*, 2010, **58**(4), p 1455–1465. <https://doi.org/10.1016/j.actamat.2009.10.053>
127. X. Li and W. Tan, Numerical Investigation of Effects of Nucleation Mechanisms on Grain Structure in Metal Additive Manufacturing, *Comput. Mater. Sci.*, 2018, **153**, p 159–169. <https://doi.org/10.1016/j.commatsci.2018.06.019>
128. R. Shi, S.A. Khairallah, T.T. Roehling, T.W. Heo, J.T. McKeown and M.J. Matthews, Microstructural Control in Metal Laser Powder Bed Fusion Additive Manufacturing Using Laser Beam Shaping Strategy, *Acta Mater.*, 2020, **184**, p 284–305. <https://doi.org/10.1016/j.actamat.2019.11.053>
129. T. Pinomaa, M. Lindroos, M. Walbrühl, N. Provatas and A. Laukkanen, The Significance of Spatial Length Scales and Solute Segregation in Strengthening Rapid Solidification Microstructures of 316L Stainless Steel, *Acta Mater.*, 2020, **184**, p 1–16. <https://doi.org/10.1016/j.actamat.2019.10.044>
130. W. Chen, “A Computational Multiscale Integrated Model for Microstructure Simulation in Selective Laser Melting,” (Clear Water Bay, Kowloon, Hong Kong), The Hong Kong University of Science and Technology, 2016, <https://doi.org/10.14711/thesis-b1627875>
131. M. Mazur, P. Brincat, M. Leary and M. Brandt, Numerical and Experimental Evaluation of a Conformally Cooled H13 Steel Injection Mould Manufactured with Selective Laser Melting, *Int. J. Adv. Manuf. Technol.*, 2017, **93**(1–4), p 881–900. <https://doi.org/10.1007/s00170-017-0426-7>
132. Schmolz + Bickenbach, “P-20 High Hardness Plastic Mold Steel,” *MatWeb*, n.d., <http://www.matweb.com/search/DataSheet.aspx?MatGUID=ed034a5881774162a0f2e4ce26188efb>. Accessed from 29 Apr 2021
133. Additively, “Laser Melting (LM),” n.d., <https://www.additively.com/en/learn-about/laser-melting>. Accessed from 20 Feb 2021
134. Additively, “Electron Beam Melting (EBM),” n.d., <https://www.additively.com/en/learn-about/electron-beam-melting>. Accessed from 20 Feb 2021
135. 3Diligent, “Directed Energy Deposition Service at a Glance,” n.d., <https://www.3diligent.com/prodex/manufacturing-services/3d-printing-service/directed-energy-deposition/>. Accessed from 20 Feb 2021

Publisher's Note Springer Nature remains neutral with regard to jurisdictional claims in published maps and institutional affiliations.